RSC Advances

ROYAL SOCIETY OF CHEMISTRY

www.rsc.org/advances

Journal Name RSCPublishing

ARTICLE

A new method to prepare vanadium oxide nano-urchins as cathode for lithium ions battery

Cite this: DOI: 10.1039/x0xx00000x

Received 00th January 2012,
Accepted 00th January 2012

DOI: 10.1039/x0xx00000x

www.rsc.org/

Jichao Wang,[a] Chaojun Cui,[a] Guohua Gao,*[a] Xiaowei Zhou,[a] Jiandong Wu,[a] Huiyu Yang,[a] Qiang Li,[a] Guangming Wu*[a]

Urchin-like vanadium oxide nanotubes clusters abbreviated to VO_x-NUs are synthesized via using a new method. Vanadium pentoxide owning layered structure is modified by lithium fluoride (LiF) and transformed into bi-phase lithium vanadate as inorganic precursor. And then, VO_x-NUs are prepared by hydrothermal reaction with dodecylamine as template. This is different from these molecular assembly methods reported. VO_x-NUs-350 nano clusters are obtained by annealing VO_x-NUs at a temperature of 350 °C in air. Both samples are identified as three dimensional urchin-like nano clusters. Based on characterization obtained, formation mechanism is established. By varying the LiF stoichiometric ratio simply, nano tubes density of VO_x-NUs can be controlled. VO_x-NUs present a higher initial rate capacity of 400 $mAhg^{-1}$ and VO_x-NUs-350 keep a better capacity of 150 $mAhg^{-1}$ after 50 cycles at 100 mAg^{-1} current density between 1.5 and 4 V versus Li/Li^+.

Introduction

Hybrid electric vehicles (HEVs) and electric vehicles (EVs) powered by lithium-ion batteries are more and more popular among people due to economic and environmental advantage. Especially, EVs to travel remotely become potential substitutes for conventional vehicles. Also, research of lithium-ion battery electrode materials with large capacity is urgent for popularity of large-screen mobile devices. But the specific capacity and energy density of current lithium-ion battery are too small to meet current requirements.

Vanadium oxide has been widely studied due to excellent electrochemical and catalytic performance. Vanadium pentoxide is considered to have the highest theoretical capacity and be a promising cathode material for high-capacity lithium-ion battery[1]. However, due to irreversibility of crystalline phases with ions insertion and extraction, poor ions conductivity and active materials solubility in the electrolyte, modified nanostructured vanadium oxide materials[2-4] are used as new kinds of electrode materials. Nanostructured vanadium oxide can significantly improve these properties because of higher surface area and shorter Li^+ ion diffusion distance[5, 6]. A variety of one-dimensional nanostructured vanadium oxides have been synthesized[7-9]. Even so, low-dimensional nano-materials are delivering the same disadvantage of dispersibility (self-aggregation) due to higher surface energy[10-12]. More orderly three dimensional vanadium oxide materials, such as nano-flowers[13-16], nano-urchins [17-20] and nano-crusts[21], are synthesized by hydrothermal method or alcothermal method to overcome this problem. By retaining large particles and reducing contact area between electrodes and electrolytes, less dissolution than one-dimensional materials and higher volumetric energy densities are obtained[22]. Vanadium oxide nano-urchins have been prepared typically by using costly organic vanadium sources [23] or complicated cations-induced inorganic vanadium sources [18] in combination with templates.

In this paper, a new approach with low-cost inorganic precursors is proposed. It's different from these molecular assembly methods above. Nano-urchins (VO_x-NUs) are synthesized by hydrothermal method based on traditional curling mechanism[24], and nano-tube clusters density is relative to LiF stoichiometric ratio. VO_x-NUs is calcined at 350 °C in air to produce urchin-like V_2O_5 nano crystal clusters abbreviated to VO_x-NUs-350. Morphology, structure and electrochemical characterization of VO_x-NUs and VO_x-NUs-350 are preliminarily indicated.

Experimental

The synthesis was performed following the methods of solid-state reaction and hydrothermal treatment. First, starting materials with different stoichiometric proportion (molar ratios of V_2O_5 and LiF were 1:0.3 and 1:0.4) were transferred to different porcelain crucibles respectively, and then put in muffle furnaces. The muffle furnaces were heated to 700 °C at the heating rate of 5 °C•min^{-1}, and kept at 700°C for 2~4h. The melted compounds were left to cool naturally and then modified precursors were obtained and denoted by 0.3LiF+VO_x and 0.4LiF+VO_x[25]. These as-synthesized precursors were ground into powder by ball milling. Second, hydrothermal procedure was similar to those reported in literature[26, 27]. 1 g modified precursors αLiF+VO_x powder and 1.04g dodecylamine were slowly added in 80 mL deionized water under magnetic stirring about 30 min, which led to the formation of yellow suspension liquid. The yellow suspension liquid was vigorously stirred for 12 h and transferred into a 100 mLTeflon-lined hydrothermal autoclave with a stainless steel shell. The autoclaves were kept at 180 °C in an oven for 7 days. The precipitate obtained was filtered, and rinsed repeatedly with ethanol and deionized water,

then dried at 70 °C under vacuum for 8 h. The resulting black powders were urchin-like vanadium oxide nanotube clusters (VO_x-NUs). 0.3VO_x-NUs was the product of precursor 0.3LiF+VO_x and 0.4VO_x-NUs was the product of precursor 0.4LiF+VO_x. VO_x-NUs-350 nano crystal clusters were obtained by annealing VO_x-NUs at a temperature of 350 °C for 3 h in air with a heating rate of 5 °C min^{-1} and denoted by 0.3VO_x-NUs-350 and 0.4VO_x-NUs-350.

Scanning Electron Microscopy (SEM: Philips-XL-30FEG) and Transmission electron microscope (TEM: 200 kV JEOL-1230) were introduced to observe morphologies and characterize the microstructure of samples with very high spatial resolution. X-ray powder diffraction (XRD) patterns were obtained by using a RigataD/max-C diffractometer with CuK_α radiation source (λ= 1.5406 Å) in range of 5-60 º for phase identification. FT-IR absorption spectroscopy measurements were carried out using a Bruker-TENSOR27 FTIR spectrometer in range of 400–4000 cm^{-1} to characterize surface chemical-physical properties by KBr disk method. The thermogravimetry (TG) and differential scanning calorimeter (DSC) measurements were performed on a SDT Q600 in the temperature range of 17-650 °C with a heating rate of 10 °C min^{-1} in air atmosphere. XPS experiments were conducted on a RBD upgraded PHI-5000C ESCA system (Perkin Elmer) with Mg Kα radiation (hυ = 1253.6 eV). Binding energies were calibrated by using the containment carbon (C_{1s}=284.6 eV). The data analysis was carried out by using XPS Peak4.1 software.

The cathode electrodes for electrochemical characterization were prepared by mixing active materials with carbon black and polyvinylidene fluoride (PVDF) binder (70:20:10 wt%) in N-methyl-2-pyrrolidone (NMP) solvent. And then the obtained slurry was uniformly coated on an aluminum foil current collector. The electrodes were dried in vacuum at 120 °C for 8 h, and then cut into circular wafer for test, with a microporous film (Celgard2500) as membrane and lithium metal as anode and reference electrode in model CR2025 coin cells. The electrolyte was 1 M $LiPF_6$ dissolved in ethylene carbonate (EC) / dimethyl carbonate (DMC) / diethyl carbonate (DEC) (1:1:1 in volume). The coin cells were assembled in an argon-filled glove box with moisture content and oxygen level less than 1 ppm. The electrochemical tests were performed by using LAND cell-testing system and CHI660C electrochemical workstation at the room temperature. Cyclic voltametry (CV) measurements were done at a scanning rate of 0.1 mV s^{-1}. Electrochemical impedance spectroscopy (EIS) measurements were carried out in frequency range between 100 kHz and 0.01 Hz at a discharge state of 2.3 V, with 5mV as amplitude of the AC signal. The impedance data were analyzed using Z-view software and fitted based on the simple equivalent circuit. Galvanostatic charge/discharge tests were recorded within a voltage range of 1.5-4.0 V (vs. Li/Li^+), at a charge/discharge current of 100 mA g^{-1}.

Results and discussion

Fig.1a and Fig.1b in Figure 1 are SEM and TEM images of 0.3VO_x-NUs respectively which has been prepared with as-synthesized 0.3LiF+V_2O_5. As can be seen in Fig.1a, 0.3VO_x-NUs shows a sea urchin-like three-dimensional configuration with pin-like vanadium oxide nanotubes over it. Large quantity of open-end nanotubes (~1 μm) are evident. These dense nano-tubes clusters have diameters in the range of 2~3 μm. Internal structure of nano-urchins can be further seen in TEM diagrams (Fig.1b). Expand from a center, dense nano-tubes uniformly spread out in Fig.1b inset. Fig.1b shows one single nano-tube from nano-urchins, which maintains a complete nano-tube structure. Its outside diameter is greater than 60 nm and inside diameter is about 20 nm. The interlamellar distance is 2 nm clearly. The interlamellar distance reflects the two-dimensional structure of VO_x layers and the 2 nm spacing corresponds to reflection 001.[28] Fig.1c and Fig.1d show the SEM and TEM of 0.4VO_x-NUs prepared with as-synthesized 0.4LiF+V_2O_5. Compared with 0.3VO_x-NUs, 0.4VO_x-NUs also present a three-dimensional configuration of nano-urchins in Fig.1c and Fig.1d inset.

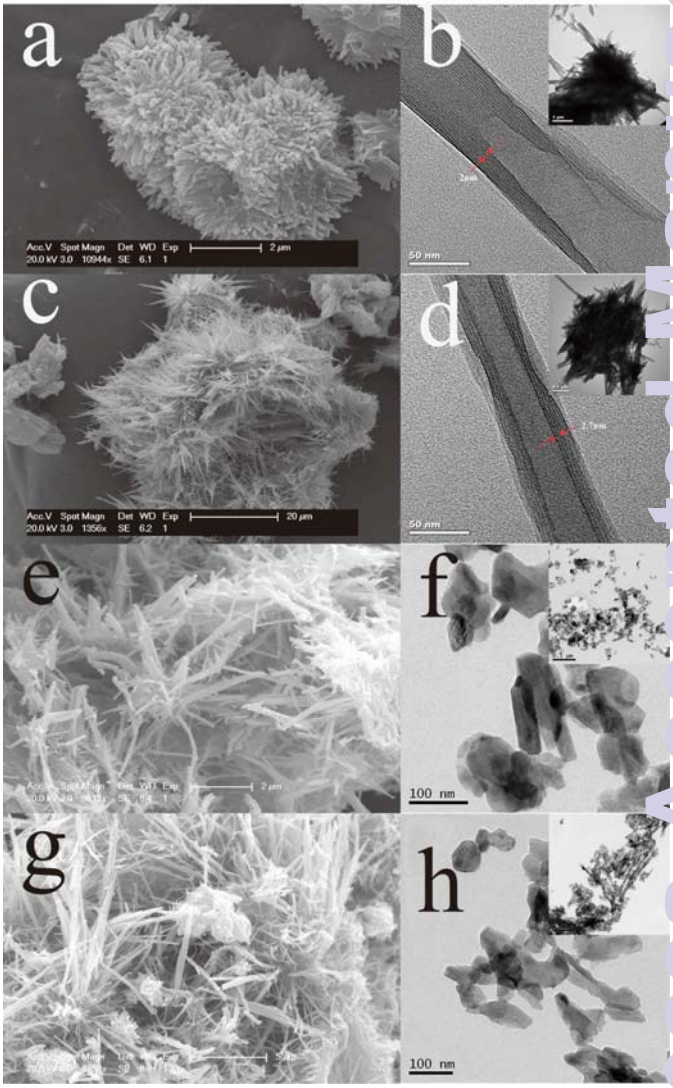

Fig.1. SEM image (a) and TEM image (b) of 0.3VO_x-NUs. SEM image (c) and TEM image (d) of 0.4VO_x-NUs. SEM image (e) and TEM image (f) of 0.3VO_x-NUs-350. SEM image (g) and TEM image (h) of 0.4VO_x-NUs-350. Inset: low magnification TEM images.

However, the nano-tubes volumetric density of 0.4VO_x-NUs is lower than 0.3VO_x-NUs, as seen in Fig.1a and Fig.1c. 0.4VO_x-NUs nano-tubes clusters have larger diameters in the range of 15~20 μm and longer nanotubes (~10 μm). Fig.1d displays a single nano-tube of 0.4VO_x-NUs. Tube walls locally collapse, outside diameter is less than 60nm, and inside diameter is about 27nm. Nano-tube structure remains intact and interlamellar distance expands to 2.7nm. It is illustrated that LiF is influential

on the three dimensional structure, but also on the structure of single nano-tube.

Fig.1e and Fig.1f show that urchin-like configuration and building nano-blocks of 0.3VO_x-NUs-350. It can be seen that 0.3VO_x-NUs-350 synthesized by sintering 0.3VO_x-NUs is composed of small interconnected nano-blocks with size of 50~100 nm. These nano-urchin clusters also have diameters in the range of 2~3 μm and lower volumetric density nano-pin over them. The same things happen to 0.4VO_x-NUs-350 with larger clusters diameters of 15~20 μm in Fig.1g and Fig.1h.

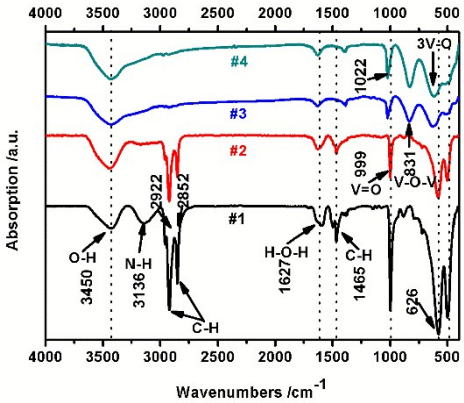

Fig.2. FT-IR spectra of 0.3VO_x-NUs (#1), 0.4VO_x-NUs (#2), 0.3VO_x-NUs-350 (#3) and 0.4VO_x-NUs-350 (#4).

As seen in FTIR spectrum of Fig.2, VO_x-NUs and VO_x-NUs-350 present some difference characteristic vibration peaks, especially in region of end group oxygen [29]. The absorption peaks at 1465, 2852, and 2922 cm^{-1} are assigned to the various bending and stretching modes of C-H vibrations in dodecylamine for VO_x-NUs. These peaks totally disappear for V_2O_5-NUs-350, indicating the complete removal of dodecylamine after sintering. Two peaks at 1627 and 3450 cm^{-1} are attributed to H-O stretching and H-O-H bending vibration modes. For all samples, the characteristic peaks near 1000 cm^{-1} (999 and 1022 cm^{-1}), ranging from 700 to 900 cm^{-1} (831 cm^{-1}) and below 700 cm^{-1} (499, 626 and 630 cm^{-1}) correspond to the stretching vibration of terminal oxygen bonds (V=O), the vibration of doubly coordinated oxygen bonds (O-V-O), and the asymmetric and symmetric stretching vibrations of triply coordinated oxygen bonds in vanadium oxide (3V-O), respectively[27, 30]. The shifting of corresponding coordinated oxygen bonds may be caused by the lattice distortion and microscopic stress variation in coordination geometry. LiF characteristic peaks are not found in Fig.2. It is believed that LiF had been removed during sintering process[25] and hydrothermal process. Although nano-urchins don't present additional absorption peaks contrast to VO_x-NTs[30], LiF does modify precursors and has an impact on the final morphology according to SEM and TEM above.

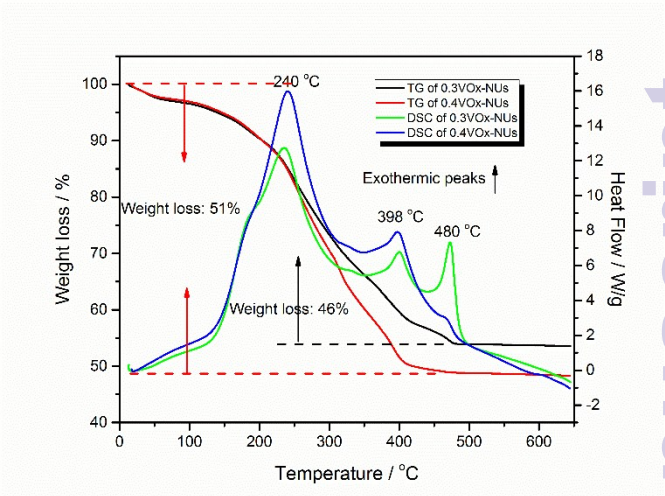

Fig. 3. TG-DSC curves of αVO_x-NUs (α=0.3, 0.4) in air.

Fig. 3 gives the TG-DSC curves of VO_x-NUs in air. Weight loss of 10% from the room temperature to about 200 °C is assigned to the thermal evaporation of absorbed water molecules. The thorough oxidative decomposition of organic templates for VO_x-NUs is completed at 450 °C, causing total 51% of weight loss which will describe the approximate content of organic templates in VO_x-NUs. The exothermic peaks at 240 °C can be ascribed to the decomposition of dodecylamine. Two exothermic peaks at 398 °C and 480 °C can mainly be ascribed to recrystallization of VO_x layers. The organic templates will mostly be removed at 350 °C and recrystallization won't happen down to the changes of nanostructures.

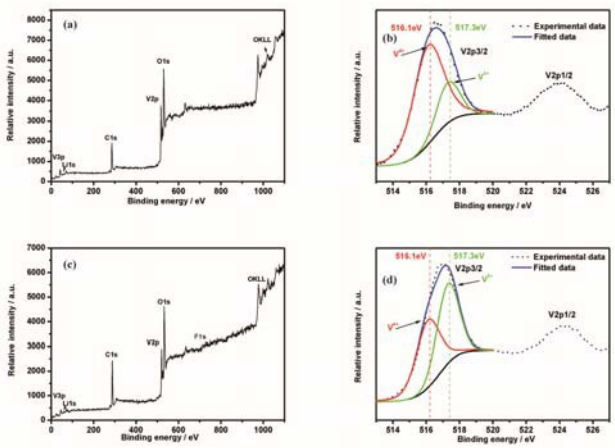

Fig. 4. XPS general spectrum and V_{2p} region of 0.3LiF+VO_x (a, b) and 0.4LiF+VO_x (c, d)

XPS technique is employed to identify the element component of αLiF+VO_x (α=0.3, 0.4) and analyze the content of vanadium element with different valence states. The XPS general spectrum of αLiF+VO_x is given in Fig. 4(a, c). The F_{1s} peak at about 690 eV originates from LiF is too weak to identify.

Fig. 4(b, d) present the V_{2p} region of XPS spectrum, which include the $V_{2p3/2}$ and $V_{2p1/2}$ peaks, and $V_{2p3/2}$ peak can be divided into two peaks at the binding energies of 517.3 and 516.1 eV which are ascribed to V^{5+} and V^{4+}, respectively. As shown in Fig. 4(b, d), XPS Peak4.1 software is applied to fit the experiment.

data and ascertain the ratio of V^{5+}/V^{4+} in αLiF+VO_x through the calculation of V^{5+} peak area/V^{4+} peak area. The fitted result illustrates that the ratio of V^{5+}/V^{4+} in 0.3LiF+VO_x is 0.29, that is, V^{5+} and V^{4+} account for 22.7% and 77.3%. The ratio of V^{5+}/V^{4+} in 0.4LiF+VOx is 1.02, that is, V^{5+} and V^{4+} account for 50.5% and 49.5%, respectively.
Fluorine is believed not to insert vanadium oxide layers due to the reaction of fluorine and silicon oxide which is the main components of the crucible. The reaction has been detailly described in another paper[25].

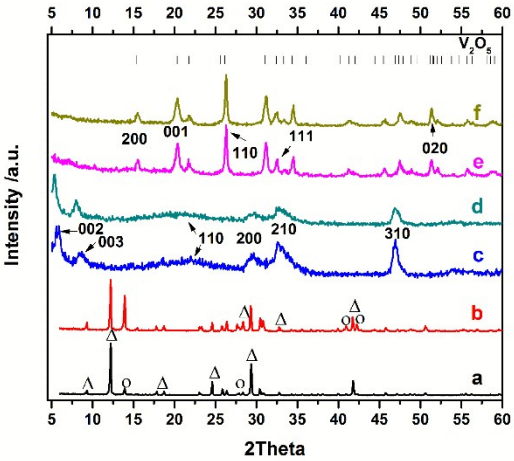

Fig. 5. XRD patterns of 0.3LiF+V_2O_5 (a), 0.4LiF+V_2O_5 (b), 0.3VO_x-NUs (c), 0.4VO_x-NUs (d), 0.3VO_x-NUs-350 (e), 0.4VO_x-NUs-350 (f) and the orthogonal V_2O_5 standard peaks (JCPDS No. 41-1426, space group: *Pmmn*, a = 11.516 Å, b = 3.566 Å, c = 4.372 Å).

XRD patterns are performed to determine the crystalline phases in Fig. 5. The black line (Fig. 5-a) is the XRD pattern of sample 0.3LiF+V_2O_5. The red line (Fig. 5-b) is for 0.4LiF+V_2O_5. It's thought that peaks marked by ○ ascribed to LiV_3O_8 phase (JCPDS card: No. 35-0437), and other strong peaks ascribe to $Li_{0.3}V_2O_5$ phase (JCPDS card: 18-0755), marked by Δ. It can be seen that LiV_3O_8 phase in 0.4LiF+V_2O_5 is stronger than 0.3LiF+V_2O_5[25]. The blue line (Fig. 5-c) and cyan line (Fig. 5-d) are the XRD patterns of 0.3VO_x-NUs and 0.4VO_x-NUs, respectively. VO_x-NUs samples can be indexed on the basis of orientation (002), (003), (110), (200), (210), and (310)[19, 20]. The Bragg reflections indicate that VO_x-NUs are lamellar intercalated products of amine and vanadium oxide. The peaks (002) and (003) with higher intensity at small angle region corroborate the interlayer distance and can be used to calculate the distance between VO_x layers[27]. According to Bragg's law, the distances are 2.8 nm for 0.3VO_x-NUs and 3 nm for 0.4VO_x-NUs, which are close to the results of TEM observation. The characteristic reflections peaks (110), (200), (210) and (310) indicate high structural order of vanadate layers, but also intercalated amine groups between these layers[20, 31]. Remarkably, the positions of hk0 reflections are same for all VO_x-NUs samples, indicating that the content of wall structure are not affected by LiF. But the (*00l*) peaks of 0.4VO_x-NUs significantly move to lower degrees than 0.3VO_x-NUs. The shifts mean that the distance of layers in 0.3VO_x-NUs is smaller than that in 0.4 VO_x-NUs. Prelithiation of V_2O_5 makes more lithium ions insertion in the vanadium oxide layers which can increase the layers spacing and is consistent with the TEM images. VO_x-NUs-350 samples display a series of characteristic diffraction peaks (200), (001), (101), (110), (111), (020), etc. which can be indexed to the orthogonal V_2O_5 phase (JCPDS No. 41-1426, space group: *Pmmn*, a = 11.516 Å, b = 3.566 Å, c = 4.372 Å), and no LiF peaks are detected, indicating the high purity of V_2O_5 nano-crystals[12, 27]. Through calculation based on Scherrer formula, the average grain size of V_2O_5 nano-crystals is ~40 nm which is in agreement with TEM and SEM observations.

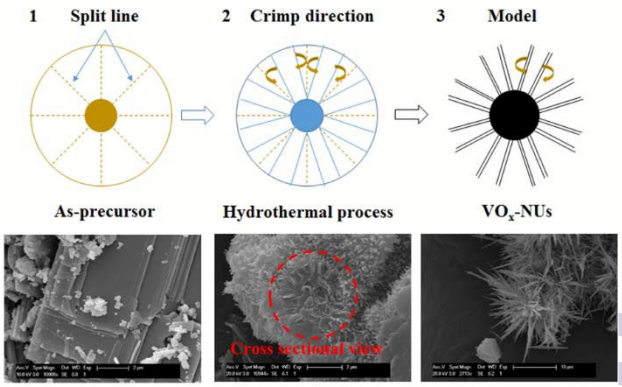

Fig. 6. Schematic diagram showing the formation of VO_x-NUs.

In Fig. 6, the formation of nano-urchins is simulated. The as-precursors are double-crystal materials known from the XRD in Ref.[25] And they are bulk materials in above SEM-1 of Fig. 6. Grain boundaries exist between different crystal substances. With the insertion of template, the layered materials produce split lines due to unbalanced stress, which are schematically shown in Fig. 6-1. In the hydrothermal process (Fig. 6-2), the fracture layers center on one point and partly curl as VO_x-NTs[9] in SEM-2 of Fig. 6. This image is a sectional view of semi-finished VO_x-NUs internal structure and nano-urchins forming state has been shown clearly. Basically it can be speculated that forming process of nano-tubes began from outside with a common center. Curling of many super imposed layers eventually form nano-urchins (Fig. 6-3). These correspond to the SEM and TEM images.

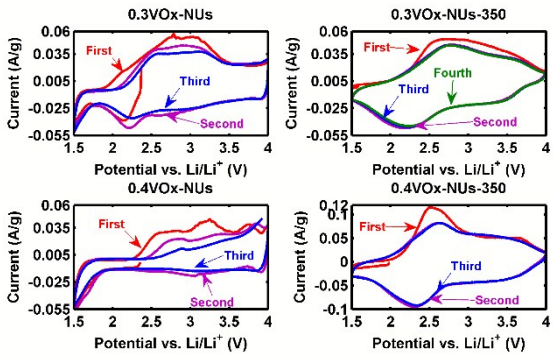

Fig. 7. Cyclic voltammogram of samples at a scan rate of 0.1 mVs^{-1} between 1.5 and 4.0 V.

Cyclic voltammetry is employed to evaluate the samples' electrochemical properties. Fig. 7 shows the initial three cycles under low scan rate of 0.1 mVs^{-1} between 1.5 and 4 V. At the first cycling of 0.3VO_x-NUs, two anodic peaks at 2.8 V and 3.1 V are observed. One cathodic peak at 2.2 V related to the lithium ions extraction is observed. At the second and third cycling, the cathodic peak move to 2.25 V and 2.3 V, respectively. For 0.3VO_x-NUs-350, one anodic peak at 2.5 V is observed and

moves to 2.7 V for the following cycles. The cathodic peak keeps at 2.25 V, indicating the good cyclability. 0.4VO_x-NUs has three anodic peaks at 2.5 V, 3.25 V and 3.75 V at the first cyclling, which become two peaks at 2.75 V and 3.4 V at the second cycling and disappear at the third cycling. It doesn't show distinct cathodic peak. 0.4VO_x-NUs-350 reveals a good cyclability as 0.3VO_x-NUs-350. One anodic peak at 2.5 V is observed and moves to 2.7 V for the following cycles. The cathodic peak keeps at 2.25 V.

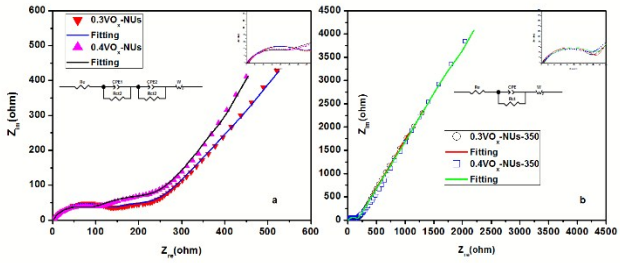

Fig. 8. Nyquist plots (a) for 0.3VO_x-NUs and 0.4VO_x-NUs and (b) for 0.3VO_x-NUs-350 and 0.4VO_x-NUs-350 with 5 mV amplitude of AC signal at the state of charge of 2.3 V (inset: equivalent circuit used for fitting the Nyquist plots and Nyquist plots magnification at high frequency region).

Electrochemical impedance spectroscopy (EIS) is introduced to evaluate the electrochemical mechanism of these samples. The typical Nyquist plots at a discharge state of 2.3 V are presented in Fig. 8(a) and (b), respectively. The plots show depressed semicircles in the high-frequency region and sloped lines in the low-frequency region. Generally, the diameter of semicircle in the high-frequency region is associated with charge transfer reaction at the electrolyte/electrode interface. The smaller the diameter of the semicircle is, the smaller the charge transfer resistance will be. The sloped line in the low-frequency region is related to the Warburg impedance associated with the ions diffusion process in the electrode materials[27, 30]. As can be seen from Fig. 8 (a) inset and (b) inset, the semicircle diameters of VO_x-NUs-350 are smaller than those of VO_x-NUs in the high-frequency region, indicating that VO_x-NUs-350 samples have lower charge transfer resistance compared to VO_x-NUs samples.

Table 1
The fitted electrolyte resistance (*R*e), charge transfer resistance (*R*ct) for the two samples at the state of charge (SOC) of 2.3 V.

Samples		0.3VO_x-NUs	0.3VO_x-NUs-350	0.4VO_x-NUs	0.4VO_x-NUs-350
Open circuit potential	*R*ct1 / Ω	123	163	88.44	163.2
	*R*ct2 / Ω	100.1		144.3	

Two simple equivalent circuits shown in the inset of Fig. 8(a) and (b) are built to analyze the impedance spectra of the samples. In the circuit, *R*e presents the electrolyte resistance, *R*ct stands for the charge transfer resistance, *CPE* is the double layer capacitance, and *W* is the Warburg impedance. The electrochemical parameters of the samples are fitted by using Z-view software, and a good agreement between experimental results and the parameters obtained from the equivalent circuit can be seen from the EIS spectra. The fitted electrochemical parameters are listed in Table 1. As can be seen from Table 1, the charge transfer resistances (*R*ct) for 0.3VO_x-NUs and 0.4VO_x-NUs at open circuit potential are *R*ct1+*R*ct2, 223.1 ohm and 232.74 ohm, respectively. The charge transfer resistances (*R*ct) for 0.3VO_x-NUs-350 and 0.4VO_x-NUs-350 are 163 ohm and 163.2 ohm. It is clear that the *R*ct values of VO_x-NUs-350 samples are much smaller than that of VO_x-NUs samples, indicating that charge transfer is easier for VO_x-NUs-350 samples than VO_x-NUs.

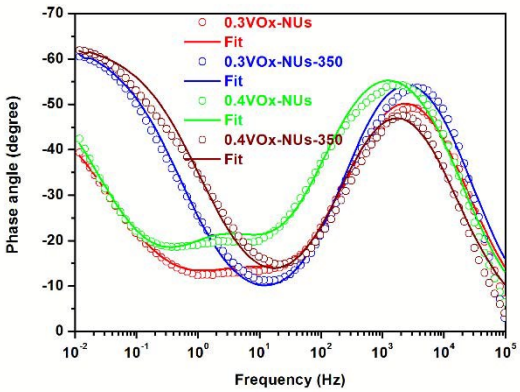

Fig. 9. Bode plots of samples at open circuit potential 2.3 V.

The Bode plots in Fig. 9 can be used to estimate the effectiveness of lithium-ions diffusion in the electrode materials. According to Ref.[25, 32], the lithium-ions diffusion is related to the phase angle at the low-frequency region. The smaller the phase angle is, the faster the lithium-ions diffusion is. As shown in Fig.9, the phase angles of VO_x-NUs-350 samples are much smaller than that of VO_x-NUs samples at the low-frequency region, indicating that VO_x-NUs-350 samples have more rapid lithium-ions diffusion speeds than that of VO_x-NUs samples. The improved electrochemical kinetics may be attributed to the removing of organic template according to FT-IR in Fig. 2.

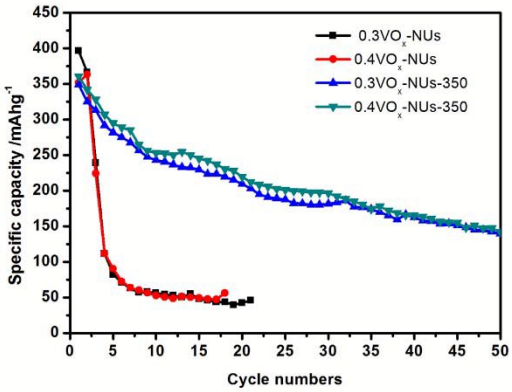

Fig. 10. Galvanostatic cycles of 0.3VO_x-NUs, 0.4VO_x-NUs, 0.3VO_x-NUs-350 and 0.4VO_x-NUs-350 at current density of 100 mA/g between 1.5 and 4 V.

Discharge capacities versus cycle numbers of VO_x-NUs and VO_x-NUs-350 are plotted in Fig. 10, at a constant current density of 100mA/g between 1.5 and 4.0 V vs Li/Li^+. 0.3VO_x-NUs and 0.4 VO_x-NUs deliver the initial specific capacities of 396.4 mA h / g and 351.9 mA h / g, respectively. After 20 cycles, they remain the capacities of 40 and 50 mA h / g. The initial capacity values for 0.3VO_x-NUs-350 and 0.4 VO_x-NUs-350 are 366.3 and 363.5 mA h / g, respectively. After 50 cycles, both fade to about 150 mA h / g. The rapid capacity decay of VO_x-NUs may be caused by the decomposition of organic dodecylamine and its severe contamination to electrolyte. It can be concluded that nano urchin-like VO_x-NUs-350, which is composed of interconnected V_2O_5 nanocrystals and free of organic templates, possesses high specific capacity and superior cycling performance.

Conclusions

Two species nano-urchins of vanadium oxide are prepared by a new method involving bi-phase lithium vanadate materials and hydrothermal method with dodecylamine. SEM and TEM show that evident structure and configuration of nano-urchins. XRD and FT-IR confirm that components of nano-urchins are nano-tubes, which V_2O_5 nanocrystals will substitute for after sintering. Both VO_x-NUs and VO_x-NUs-350 samples exhibit excellent initial discharge specific capacity of about 400 $mAhg^{-1}$ at 100 mAg^{-1} current density between 1.5 and 4 V versus Li/Li^+. However, VO_x-NUs-350 samples possess outstanding cycling performance a better capacity of 150 $mAhg^{-1}$ after 50 cycles due to removing of organic template.

Acknowledgements

The authors gratefully acknowledge the financial support from the Shanghai Committee of Science and Technology (11nm0501300 and 13JC1408700), the National Natural Science Foundation of China (51472182, 51272179 and 51102183).

Notes and references

[a] *Shanghai Key Laboratory of Special Artificial Microstructure Materials and Technology, Tongji University, Shanghai 200092, P.R. China.*
**E-mail: gao@tongji.edu.cn, wugm@tongji.edu.cn; Fax: +86-21-6598-6071; Tel: +86-21-6598-2762*

1. M. S. Whittingham, *Chem Rev*, 2004, **104**, 4271-4301.
2. X. L. Jia, L. Q. Zhang, R. F. Zhang, Y. F. Lu and F. Wei, *Rsc Adv*, 2014, **4**, 21018-21022.
3. Z. L. Li, Q. Y. Zhu, S. N. Huang, S. S. Jiang, S. Lu, W. Chen and G. S. Zakharova, *Rsc Adv*, 2014, **4**, 46624-46630.
4. B. Saravanakumar, K. K. Purushothaman and G. Muralidharan, *Rsc Adv*, 2014, **4**, 37437-37445.
5. R. S. Devan, R. A. Patil, J. H. Lin and Y. R. Ma, *Adv Funct Mater*, 2012, **22**, 3326-3370.
6. M. Shahid, D. S. Rhen, I. Shakir, S. P. Patole, J. B. Yoo, S. J. Yang and D. J. Kang, *Mater Lett*, 2010, **64**, 2458-2461.
7. J. Livage, *Materials*, 2010, **3**, 4175-4195.
8. F. Sediri, F. Touati and N. Gharbi, *Mater Lett*, 2007, **61**, 1946-1950.
9. W. Chen, J. F. Peng, L. Q. Mai, Q. Y. Zhu and Q. Xu, *Mater Lett*, 2004, **58**, 2275-2278.
10. Y. G. Guo, J. S. Hu and L. J. Wan, *Adv Mater*, 2008, **20**, 2878-2887.
11. L. Q. Mai, L. Xu, C. H. Han, X. Xu, Y. Z. Luo, S. Y. Zhao and Y. L. Zhao, *Nano Lett*, 2010, **10**, 4750-4755.
12. A. Q. Pan, H. B. Wu, L. Yu, T. Zhu and X. W. Lou, *Acs Appl Mater Inter*, 2012, **4**, 3874-3879.
13. H. Yu, X. Rui, H. Tan, J. Chen, X. Huang, C. Xu, W. Liu, D. Y. W. Yu, H. H. Hng, H. E. Hoster and Q. Yan, *Nanoscale*, 2013, **5**, 4937-4943.
14. Y. X. Tang, X. H. Rui, Y. Y. Zhang, T. M. Lim, Z. L. Dong, H. H. Hng, X. D. Chen, Q. Y. Yan and Z. Chen, *J Mater Chem A*, 2013, **1**, 82-88.
15. H. H. Yin, K. Yu, Z. L. Zhang, M. Zeng, L. Lou and Z. Q. Zhu, *Electroanal*, 2011, **23**, 1752-1758.
16. H. Fei, Y. Lin and M. Wei, *Journal of Colloid and Interface Science*, 2014, **425**, 1-4.
17. M. Roppolo, C. B. Jacobs, S. Upreti, N. A. Chernova and M. S. Whittingham, *J Mater Sci*, 2008, **43**, 4742-4748.
18. H. L. Fei, Z. R. Shen, J. G. Wang, H. J. Zhou, D. T. Ding and T. H. Chen, *Electrochem Commun*, 2008, **10**, 1541-1544.
19. C. O'Dwyer, V. Lavayen, S. B. Newcomb, E. Benavente, M. A. Santa Ana, G. Gonzalez and C. M. S. Torres, *Electrochem Solid St*, 2007, **10**, A111-A114.
20. C. O'Dwyer, D. Navas, V. Lavayen, E. Benavente, M. A. Santa Ana, G. Gonzalez, S. B. Newcomb and C. M. S. Torres, *Chem Mater*, 2006, **18**, 3016-3022.
21. Q. Song, H. C. Pang, W. T. Gong, G. L. Ning, S. Gao, X. L. Dong, C. J. Liu, J. Y. Tian and Y. Lin, *Rsc Adv*, 2015, **5**, 4256-4260.
22. A. S. Arico, P. Bruce, B. Scrosati, J. M. Tarascon and W. Van Schalkwijk, *Nature materials*, 2005, **4**, 366-377.
23. V. Lavayen, C. O'Dwyer, M. A. Santa Ana, S. B. Newcomb, E. Benavente, G. Gonzalez and C. M. S. TorreS, *Phys Status Solidi B*, 2006, **243**, 3285-3289.
24. M. Niederberger, H. J. Muhr, F. Krumeich, F. Bieri, D. Gunther and R. Nesper, *Chem Mater*, 2000, **12**, 1995-2000.
25. J. Wang, G. Gao, X. Zhou, J. Wu, H. Yang, Q. Li and G. Wu, *Journal of Solid State Electrochemistry*, 2014, **18**, 2459-2467.
26. C. J. Cui, G. M. Wu, J. Shen, B. Zhou, Z. H. Zhang, H. Y. Yang and S. F. She, *Electrochim Acta*, 2010, **55**, 2536-2541.
27. X. Zhou, C. Cui, G. Wu, H. Yang, J. Wu, J. Wang and G. Gao, *J Power Sources*, 2013, **238**, 95-102.
28. F. Krumeich, H. J. Muhr, M. Niederberger, F. Bieri, B. Schnyder and R. Nesper, *J Am Chem Soc*, 1999, **121**, 8324-8331.
29. A. Surca and B. Orel, *Electrochim Acta*, 1999, **44**, 3051-3057.
30. C.-J. Cui, G.-M. Wu, H.-Y. Yang, S.-F. She, J. Shen, B. Zhou and Z.-H. Zhang, *Electrochim Acta*, 2010, **55**, 8870-8875.
31. M. Worle, F. Krumeich, F. Bieri, H. J. Muhr and R. Nesper, *Z Anorg Allg Chem*, 2002, **628**, 2778-2784.
32. C. Cui, G. Wu, H. Yang, S. She, J. Shen, B. Zhou and Z. Zhang, *Solid State Communications*, 2010, **150**, 1807-1811.

A new method to prepare vanadium oxide nano-urchins as cathode for lithium ions battery

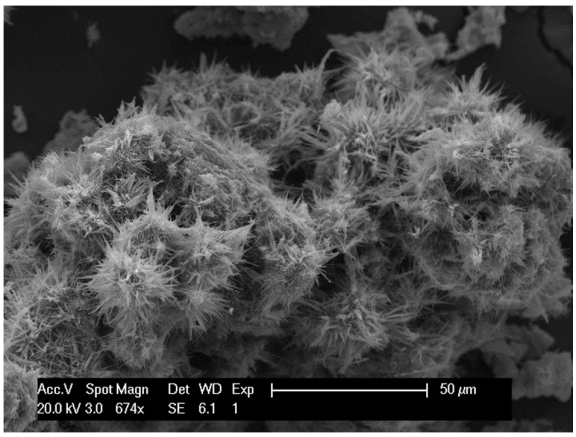

VO_x-NUs

Urchin-like vanadium oxide nanotubes clusters abbreviated to VO_x-NUs are synthesized via using a new method. Vanadium pentoxide owning layered structure is modified by lithium fluoride (LiF) and transformed into bi-phase lithium vanadate as inorganic precursor. And then, VO_x-NUs are prepared by hydrothermal reaction with dodecylamine as template. This is different from these molecular assembly methods reported. VOx-NUs-350 nano clusters are obtained by annealing VO_x-NUs at a temperature of 350 °C in air. Both samples are identified as three dimensional urchin-like nano clusters. Based on characterization obtained, formation mechanism is established. By varying the LiF stoichiometric ratio simply, nano tubes density of VO_x-NUs can be controlled. VO_x-NUs present a higher initial rate capacity of 400 $mAhg^{-1}$ and VO_x-NUs-350 keep a better capacity of 150 $mAhg^{-1}$ after 50 cycles at 100 mAg^{-1} current density between 1.5 and 4 V versus Li/Li^+.

A graphical and textual abstract for the contents pages